Absence of electron transfer-associated changes in the time-dependent X-ray free-electron laser structures of the photosynthetic reaction center

Gai Nishikawa [1], Yu Sugo [1], Keisuke Saito [1,2], and Hiroshi Ishikita [1,2]*

1) Department of Applied Chemistry, The University of Tokyo, 7-3-1 Hongo, Bunkyo-ku, Tokyo 113-8654, Japan

2) Research Center for Advanced Science and Technology, The University of Tokyo, 4-6-1 Komaba, Meguro-ku, Tokyo 153-8904, Japan

CORRESPONDING AUTHOR: Ishikita, Research Center for Advanced Science and Technology, The University of Tokyo, 4-6-1 Komaba, Meguro-ku, Tokyo 153-8904, Japan, Tel. +81-3-5452-5056, Fax. +81-3-5452-5083, **E-mail:** hiro@appchem.t.u-tokyo.ac.jp

ABSTRACT

Using the X-ray free-electron laser (XFEL) structures of the photosynthetic reaction center from *Blastochloris viridis* that show light-induced time-dependent structural changes [Dods, R.et al. (2021) Nature *589*, 310-314], we investigated time-dependent changes in the energetics of the electron transfer pathway, considering the entire protein environment of the protein structures and titrating the redox active sites in the presence of all fully equilibrated titratable residues. In the dark and charge-separation intermediate structures, the calculated redox potential (E_m) values for the accessory bacteriochlorophyll and bacteriopheophytin in the electron-transfer active branch (B_L and H_L) are higher than those in the electron-transfer inactive branch (B_M and H_M). However, the stabilization of the $[P_LP_M]^{\bullet+}H_L^{\bullet-}$ state owing to protein reorganization is not clearly observed in the $E_m(H_L)$ values in the charge-separated 5-ps ($[P_LP_M]^{\bullet+}H_L^{\bullet-}$ state) structure. Furthermore, the expected chlorin ring deformation upon formation of $H_L^{\bullet-}$ (saddling mode) is absent in the H_L geometry of the original 5-ps structure. These findings suggest that there is no clear link between the time-dependent structural changes and the electron transfer events in the XFEL structures.

INTRODUCTION

Photosynthetic reaction centers from purple bacteria (PbRC) are heterodimeric reaction centers, which are formed by the protein subunits L and M (Figure 1). In PbRC from *Blastochloris viridis*, the electronic excitation of the bacteriochlorophyll *b* (BChl*b*) pair, $[P_LP_M]$, leads to electron transfer to accessory BChl*b*, B_L, followed by electron transfer via bacteriopheophytin *b* (BPheo*b*), H_L, to menaquinone, Q_A, along the electron-transfer active L branch (A branch) [1]. Electron transfer further proceeds from Q_A to ubiquinone, Q_B, which is coupled with proton transfer via charged and polar residues in the Q_B binding region [2]. Although the counterpart M branch (B branch) is essentially electron-transfer inactive, mutations of the Phe-L181/Tyr-M208 pair to tyrosine/phenylalanine lead to an increase in the yield of $[P_LP_M]^{\bullet+}H_M^{\bullet-}$ formation (~30%), which suggests that these residues are responsible for the energetic asymmetry in the electron transfer branches (e.g., [3]). The anionic states $B_L^{\bullet-}$, $H_L^{\bullet-}$, and $Q_A^{\bullet-}$ form in ~3.5 ps, ~5 ps, and ~200 ps upon the formation of the electronically excited $[P_LP_M]^*$ state, respectively [4]. The anionic state formation induces not only reoriganization of the protein environment [5] but also out-of-plane distortion of the chlorin ring [6]. Indeed, two distinct conformations of $H_L^{\bullet-}$ were reported in spectroscopic studies of PbRC from *Rhodobacter sphaeroides* [7].

Recently, using the X-ray free electron laser (XFEL), light-induced electron density changes and structural changes of PbRC were analyzed at 1 ps, 5 ps, 20 ps, 300 ps, and 8 μs upon the electronic excitation of $[P_LP_M]$ at 960 nm [8]: the 1 ps XFEL structure represents the $[P_LP_M]^*$ state, the 5 ps and 20 ps XFEL structures represent the charge-separated $[P_LP_M]^{\bullet+}H_L^{\bullet-}$ state, and the 300 ps and 8 μs XFEL structures represent the charge-separated $[P_LP_M]^{\bullet+}Q_A^{\bullet-}$ state. According to Dods et al. [8], these XFEL structures revealed how the charge-separation process was stabilized by protein conformational dynamics. However, the conclusions drawn from these XFEL structures are based on data with limited resolution. Specifically, 8 out of 9 XFEL structures have a resolution of 2.8 Å (atomic coordinates from PDB codes: 5O4C, 6ZI4, and 6ZI5 for dataset a and 6ZHW, 6ZID, 6ZI6, 6ZI9, and 6ZIA for dataset b) [8]. The data statistics may indicate that the high-resolution range of some XFEL datasets exhibits high levels of noise

(e.g., low $CC_{1/2}$). These observations raise concerns about the reliable comparison of subtle conformational changes among these XFEL structures. Hence, caution must be exercised when interpreting these XFEL structures in terms of their ability to accurately capture relevant conformational changes.

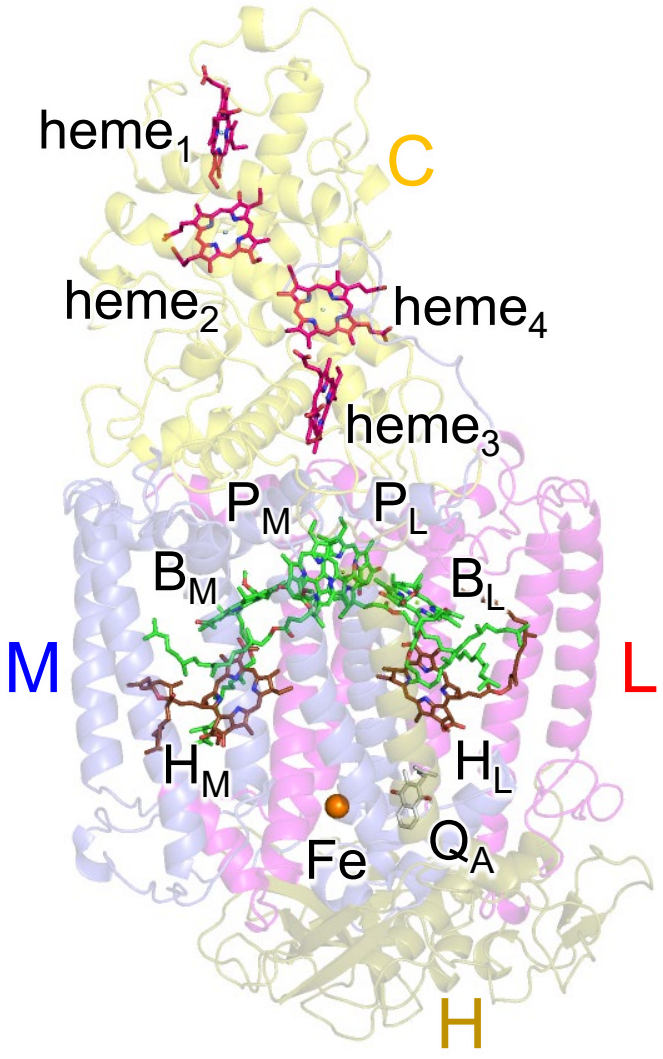

Figure 1. Electron transfer pathways along the L- and M-branches in PbRC from *Blastochloris viridis*. The PbRC is composed of the L (red), M (blue), H (gold), and C (yellow) subunits. [P_LP_M]: BChl*b* pair; B_L and B_M: accessory BChl*b*; H_L and H_M: BPheo*b*; Q_A: primary quinone (menaquinone); Fe: non-heme Fe complex.

67 Here, we investigated how the redox potential (E_m) values of the BChl*b* and BPheo*b* cofactors for one-
68 electron reduction change as electron transfer proceeds using the dark (0 ps), 1 ps, 5 ps, 20 ps, 300 ps, and
69 8 μs XFEL structures, solving the linear Poisson-Boltzmann equation, and considering the protonation
70 states of all titratable sites in the entire protein. Structural changes (e.g., side-chain orientation) in the
71 protein environment can be analyzed in the E_m shift, as E_m is predominantly determined by the sum of the
72 electrostatic interactions between the redox-active site and all other groups (i.e., residues and cofactors)
73 in the protein structure. Subtle structural changes of the BChl*b* and BPheo*b* chlorin rings, which may not
74 be pronounced even in the E_m shift [6], can be analyzed in the out-of-plane distortion of the chlorin rings
75 using a normal-coordinate structural decomposition (NSD) analysis [9, 10] with a combination of a quantum
76 mechanical/molecular mechanical (QM/MM) approach in the entire PbRC protein environment.
77

78 **METHODS**

79 **Coordinates and atomic partial charges.** The atomic coordinates of PbRC from *Blastochloris viridis*
80 were taken from the XFEL structures determined at 0 ps (dark state; PDB code 5O4C for dataset a and
81 5NJ4 for dataset b), 1 ps ($[P_LP_M]^*$ state; PDB code, 6ZHW for dataset b), 5 ps ($[P_LP_M]^{\bullet+}H_L^{\bullet-}$ state; PDB
82 code, 6ZI4 for dataset a and 6ZID for dataset b), 20 ps ($[P_LP_M]^{\bullet+}H_L^{\bullet-}$ state; PDB code, 6ZI6 for dataset
83 b), 300 ps ($[P_LP_M]^{\bullet+}Q_A^{\bullet-}$ state; PDB code, 6ZI5 for dataset a and 6ZI9 for dataset b), and 8 μs ($[P_LP_M]$
84 $^{\bullet+}Q_A^{\bullet-}$ state; PDB code, 6ZIA for dataset b). Atoms with 30% occupancy for the photoactivated state [8]
85 were used wherever present. Hydrogen atoms were generated and energetically optimized with
86 CHARMM [11]. The atomic partial charges of the amino acids were obtained from the all-atom
87 CHARMM22 [12] parameter set. For diacylglycerol, the Fe complex [13], and menaquinone [14], the atomic
88 charges were adopted from previous studies. The atomic charges of BChl*b* and BPheo*b* (BChl*b*, BChl$b^{\bullet+}$,
89 BChl$b^{\bullet-}$, BPheo*b*, and BPheo$b^{\bullet-}$) were determined by fitting the electrostatic potential in the neighborhood
90 of these molecules using the RESP procedure [15] (Tables S1). The electronic densities were calculated after
91 geometry optimization using the DFT method with the B3LYP functional and 6-31G** basis sets in the

92 JAGUAR program [16]. For the atomic charges of the nonpolar CH_n groups in the cofactors (e.g., the phytol
93 chains of BChl*b* and BPheo*b* and the isoprene side chains of quinone), a value of +0.09 was assigned to
94 nonpolar H atoms.

95 **Calculation of E_m: solving the linear Poisson-Boltzmann equation.** The E_m values in the protein
96 were determined by calculating the electrostatic energy difference between the two redox states in a
97 reference model system. This was achieved by solving the linear Poisson-Boltzmann equation with the
98 MEAD program [17] and using E_m(BChl*b*) = –665 mV and E_m(BPheo*b*) = –429 mV (based on E_m(BChl*b*)
99 = –700 mV and E_m(BPheo*b*) = –500 mV for one-electron reduction measured in dimethylformamide [18,
100 19]), considering the solvation energy difference). The $E_m(Q_A)$ value was calculated, using the reference
101 E_m value of –256 mV versus NHE for menaquinone-2 in water [20]. The difference in the E_m value of the
102 protein relative to the reference system was added to the known E_m value. To account for the ensemble of
103 protonation patterns, a Monte Carlo method with Karlsberg was used for sampling [21]. The linear Poisson-
104 Boltzmann equation was solved using a three-step grid-focusing procedure with resolutions of 2.5 Å, 1.0
105 Å, and 0.3 Å. Monte Carlo sampling provided the probabilities $[A_{ox}]$ and $[A_{red}]$ of the two redox states of
106 molecule *A*, and E_m was evaluated using the Nernst equation. A bias potential was applied to ensure an
107 equal amount of both redox states ($[A_{ox}] = [A_{red}]$), thus determining the redox midpoint potential as the
108 resulting bias potential. To ensure consistency with previous computational results, we used identical
109 computational conditions and parameters as previous studies (e.g., [13]), performing all computations at 300
110 K, pH 7.0, and an ionic strength of 100 mM. The dielectric constants were set to 4 for the protein interior
111 and 80 for water.

112 **QM/MM calculations.** We employed the restricted DFT method for describing the closed-shell electronic
113 structure and the unrestricted DFT method for the open-shell electronic structure with the B3LYP
114 functional and LACVP* basis sets using the QSite [22] program. To neutralize the entire system, counter
115 ions were added randomly around the protein using the Autoionize plugin in VMD [23]. In the QM region,
116 all atom positions were relaxed in the QM region, while the H-atom positions were relaxed in the MM

117 region. The QM regions were defined as follows: for the BChl*b* pair [P_LP_M]: the side chains of the ligand
118 residues (His-L173 and His-M200) and H-bod partners (His-L168, Tyr-M195, and Thr-L248); for
119 accessory BChl*b*: B_L/B_M and the side chain of the ligand residue (His-L153 for B_L/His-M180 for B_M); for
120 BPheo*b*: H_L/H_M.

121 **NSD analysis.** To analyze the out-of-plane distortions of chlorin rings, we employed an NSD procedure
122 with the minimal basis approximation, where the deformation profile can be represented by the six lowest-
123 frequency normal modes, i.e., ruffling (B_{1u}), saddling (B_{2u}), doming (A_{2u}), waving ($E_{g(x)}$ and $E_{g(y)}$), and
124 propellering (A_{1u}) modes [9, 10]. The NSD analysis was performed in the following three steps, as performed
125 previously [6]. First, the atomic coordinates of the Mg-substituted macrocycle were extracted from the
126 crystal (or QM/MM optimized) structure. Second, the extracted coordinates were superimposed on the
127 reference coordinates of the macrocycle. The superimposition is based on a least-square method, and the
128 mathematical procedure is described in Ref. [24]. Finally, the out-of-plane distortion in the superimposed
129 coordinates was decomposed into the six lowest-frequency normal modes by the projection to the
130 reference normal mode coordinates as

131 $$d^{\Gamma} = \sum_{i=1}^{N} \Delta z_i (n_z^{\Gamma})_i \,, \qquad \text{(Eq.1)}$$

132 where d^{Γ} represents the distortion component of the mode Γ (i.e., Γ = B_{1u}, B_{2u}, A_{2u}, $E_{g(x)}$, $E_{g(y)}$, or A_{1u}),
133 Δz_i is the *z*-component of the superimposed coordinates in the *i*th heavy atom, and $(n_z^{\Gamma})_i$ is the *z*-
134 component of the normalized eigenvector of the reference normal mode Γ in the *i*th heavy atom. *N*
135 represents the number of heavy atoms. See ref. [6] for further details.

136

137 **RESULTS AND DISCUSSION**

138 **Energetically asymmetric electron transfer branches**. The XFEL structures show that the E_m values
139 for B_L are ~50 mV higher than those for B_M, which facilitates the formation of the charge-separated [P_LP_M]
140 $^{\bullet+}B_L^{\bullet-}$ state and thereby electron transfer along the L-branch (Figures 2 and 3). As the E_m profile is

141 substantially consistent with the E_m profile for PbRC from *Rhodobacter sphaeroides* [13], it seems plausible
142 that the charge-separated $[P_LP_M]^{\bullet+}B_L^{\bullet-}$ and $[P_LP_M]^{\bullet+}H_L^{\bullet-}$ states in the active L-branch are energetically
143 lower than the $[P_LP_M]^{\bullet+}B_M^{\bullet-}$ and $[P_LP_M]^{\bullet+}H_M^{\bullet-}$ states in the inactive M-branch, respectively, as
144 demonstrated in QM/MM/PCM calculations [25]. Indeed, the calculated E_m values are largely correlated
145 with the LUMO levels calculated using a QM/MM approach, as suggested previously (coefficient of
146 determination $R^2 = 0.98$, Figure S1). The $E_m(H_L)$ value of –597 mV is in line with the experimentally
147 estimated value of ca. –600 mV for H_L in PbRC from *Blastochloris viridis* [26].

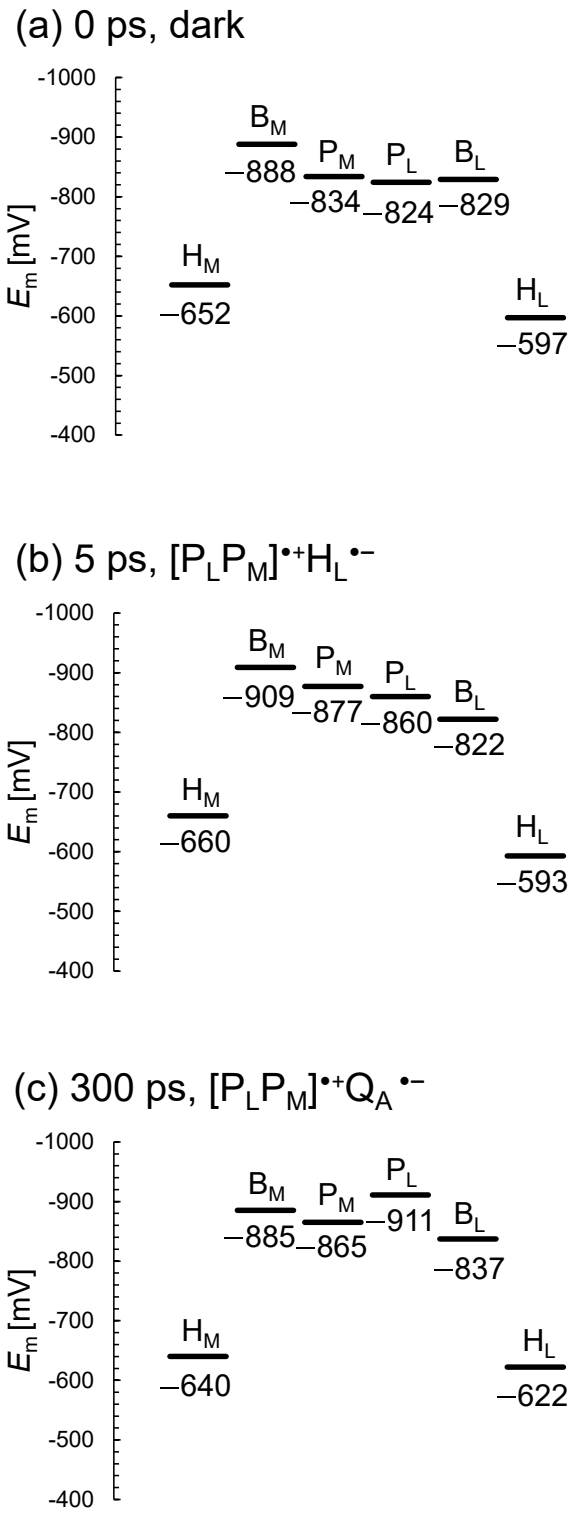

Figure 2. E_m profiles along the L- and M-branches in the XFEL structures for dataset a. (a) 0 ps. (b) 5 ps. (c) 300 ps.

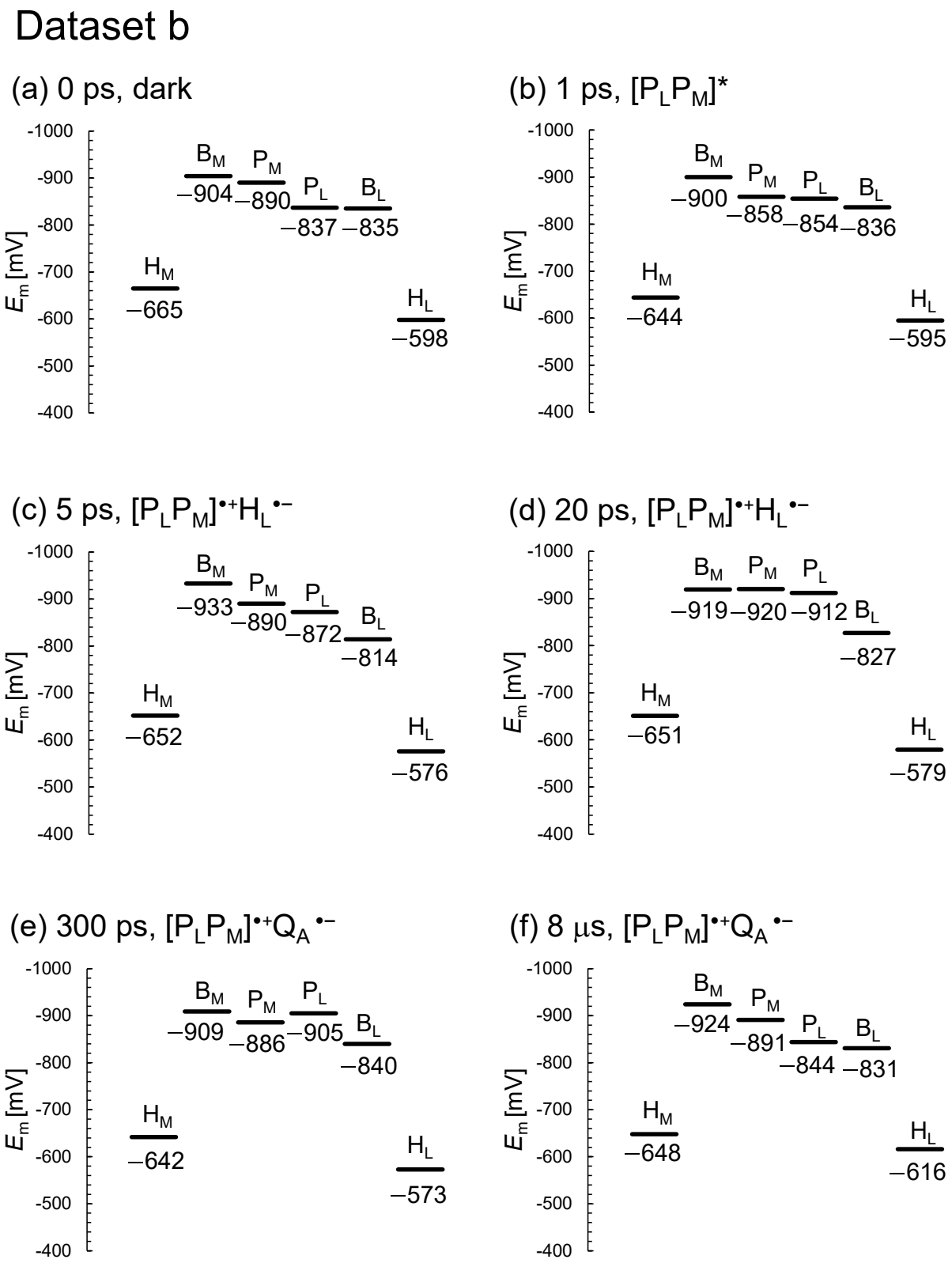

Figure 3. E_m profiles along the L- and M-branches in the XFEL structures for dataset b. (a) 0 ps. (b) 1 ps. (c) 5 ps. (d) 20 ps. (e) 300 ps. (f) 8 μs.

155

156 Among the L/M residue pairs, the Phe-L181/Tyr-M208 pair contributes to $E_m(B_L) > E_m(B_M)$ most
157 significantly (27 mV), facilitating L branch electron transfer, as suggested in theoretical studies [27] (Table
158 1, Figure 3a). This result is also consistent with the contribution of the Phe-L181/Tyr-M210 pair to the
159 difference between $E_m(B_L)$ and $E_m(B_M)$, which was the largest in PbRC from *Rhodobacter sphaeroides*
160 [28] (26 mV [13]). The Asn-L158/Thr-M185 pair also contributes to the difference between $E_m(B_L)$ and
161 $E_m(B_M)$ (11 mV, Table 1), as does the Val-L157/Thr-M186 pair in PbRC from *Rhodobacter sphaeroides*
162 (22 mV [13]).

163

164 **Table 1**. Contributions of the L/M residue pairs that are responsible for $E_m(B_L) > E_m(B_M)$ (more than 10
165 mV) in the dark-state structure (mV). Difference: [contribution of subunit L to $E_m(B_L)$] + [contribution of
166 subunit M to $E_m(B_L)$] – [contribution of subunit L to $E_m(B_M)$] – [contribution of subunit M to $E_m(B_M)$].

Subunit L	$E_m(B_L)$	$E_m(B_M)$	**Subunit M**	$E_m(B_L)$	$E_m(B_M)$	**Difference**
Phe-L181	0	17	Tyr-M208	39	-3	25
His-L144	-8	-2	Glu-M171	-14	-45	25
Asn-L158	5	-6	Thr-M185	-3	-4	12

167

168 The E_m values for H_L are ~50 mV higher than those for H_M in the dark state and [5 ps and 300 ps]
169 XFEL structures, as observed in $E_m(B_L)$ and $E_m(B_M)$ (Figure 2a,c,e). However, the E_m difference decreases
170 to ~25 mV in the [1 ps, 20 ps, and 8 μs] XFEL structures (Figure 2b,d,f), which implies that the dark state
171 and [5 ps and 300 ps] XFEL structures are distinct from the [1 ps, 20 ps, and 8 μs] XFEL structures (see
172 below). Below, we discuss the dark state structure if not otherwise specified.

173 The Ala-L120/Asn-M147 pair contributes to $E_m(H_L) > E_m(H_M)$ most significantly (38 mV) (Table 2,
174 Figure S2). However, this holds true only for PbRC from *Blastochloris viridis*, as Asn-M147 is replaced
175 with alanine (Ala-M149) in PbRC from *Rhodobacter sphaeroides*. The Asp-L218/Trp-M252 pair

decreases $E_m(H_M)$ with respect to $E_m(H_L)$, thereby contributing to $E_m(H_L) > E_m(H_M)$ (20 mV) (Table 2, Figure S2). Arg-L103 orients toward the protein interior, whereas Arg-M130 orients toward the protein exterior (Figure S2), which contributes to $E_m(H_L) > E_m(H_M)$ (17 mV) (Table 2). Ser-M271 forms an H-bond with Asn-M147 near H_M (Figure 3b). Thus, the contribution of Ser-M271 to $E_m(H_L)$ is large, although this residue is replaced with alanine (Ala-M273) in PbRC from *Rhodobacter sphaeroides*.

Table 2. Contributions of the L/M residue pairs that are responsible for $E_m(H_L) > E_m(H_M)$ (more than 10 mV) in the dark-state structure (mV). Difference: [contribution of subunit L to $E_m(H_L)$] + [contribution of subunit M to $E_m(H_L)$] – [contribution of subunit L to $E_m(H_M)$] – [contribution of subunit M to $E_m(H_M)$].

Subunit L	$E_m(H_L)$	$E_m(H_M)$	Subunit M	$E_m(H_L)$	$E_m(H_M)$	Difference
Ala-L120	-4	0	Asn-M147	0	-42	38
Asp-L218	-2	-22	Trp-M252	1	0	20
Arg-L103	77	3	Arg-M130	3	59	17
Ala-L237	-2	0	Ser-M271	3	-16	16
Lys-L110	17	2	Ala-M137	0	3	14
Val-L219	1	5	Thr-M253	17	1	11
His-L211	1	0	Arg-M245	14	4	11

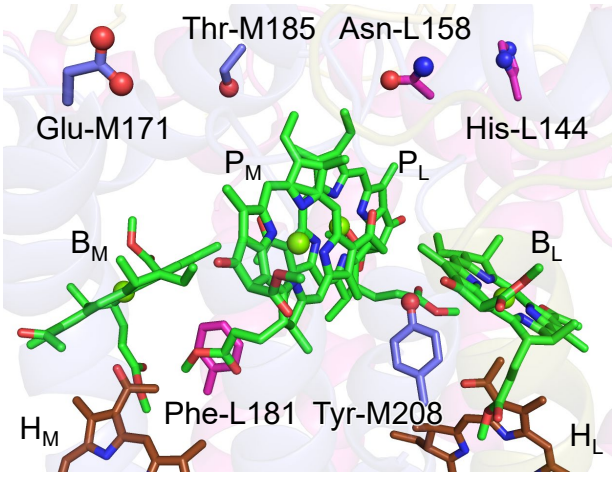

Figure 4. Residue pairs that are responsible for $E_m(B_L) > E_m(B_M)$.

189 **Relevance of structural changes observed in XFEL structures.** According to Dods et al., the 5-ps
190 and 20-ps structures correspond to the charge-separated $[P_LP_M]^{\bullet+}H_L^{\bullet-}$ state [8]. If this is the case, $E_m(H_L)$ is
191 expected to be exclusively higher in the 5-ps and 20-ps structures than in the other XFEL structures due
192 to the stabilization of the $[P_LP_M]^{\bullet+}H_L^{\bullet-}$ state by protein reorganization. In dataset a, the $E_m(H_L)$ value is
193 only 4 mV higher in the 5-ps structure than in the dark structure (Figure 5a). In dataset b, the $E_m(H_L)$ value
194 is ~20 mV higher in the 5- and 20-ps structures than in the dark structure (Figure 5b). However, the
195 $E_m(H_L)$ value is 25 mV higher in the 300-ps structure than in the dark structure. Tables 3 and 4 show the
196 residues that contribute to the slight increase in $E_m(H_L)$ most significantly in the 5- and 20-ps structures.
197 Most of these residues were in the region where Dods et al. specifically performed multiple rounds of
198 partial occupancy refinement (e.g., 153–178, 190, 230 and 236–248 of subunit L and 193–221, 232, 243–
199 253, 257–266 of subunit M) [8]. In dataset b (Table 4), which has more data points than dataset a (Table 3),
200 the contributions of these residues to $E_m(H_L)$ often fluctuate (e.g., upshift/downshift followed by
201 downshift/upshift) at different time intervals (e.g., 1 to 5 ps, 5 to 20 ps, and 20 to 300 ps). This result
202 suggests that the structural differences among the XFEL structures are not related to the actual time course
203 of charge separation. Furthermore, the $E_m(H_M)$ value in the inactive M branch is also ~15 mV higher in
204 the 5- and 20-ps structures than in the dark structure (Figure 5b). These results suggest that the ~20 mV
205 higher $E_m(H_L)$ value in the 5- and 20-ps structures is not specifically due to the formation of the
206 $[P_LP_M]^{\bullet+}H_L^{\bullet-}$ state. Thus, the stabilization of the $[P_LP_M]^{\bullet+}H_L^{\bullet-}$ state owing to protein reorganization is not
207 clearly observed in the $E_m(H_L)$ values.

208

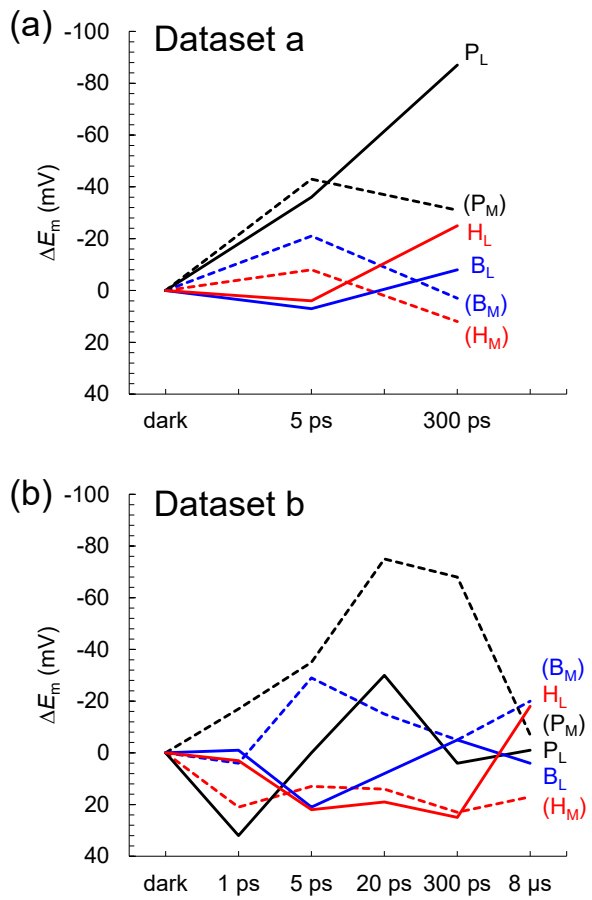

Figure 5. Time-dependent E_m changes for BChl*b* and BPheo*b* in the XFEL structures. (a) Dataset a. (b) Dataset b. ΔE_m denotes the E_m shift with respect to the dark state structure. Black solid lines: P_L; black dotted lines: P_M; blue solid lines B_L; blue dotted lines: B_M; red solid lines: H_L; red dotted lines: H_M.

Table 3. Residues that shift $E_m(H_L)$ most significantly during putative electron transfer in the XFEL structures (dataset a) (mV). The same residues are highlighted in the same colors for clarity.

Dataset a		**shift**		**shift**
0 to 5 ps	Ser-L176	5	Cys-M210	4
	Thr-M220	-7	B_L	-5
5 to 300 ps	B_L	7	Gly-M209	3
	Gly-M211	-11	Leu-M212	-8

217 **Table 4.** Residues that shift $E_m(H_L)$ most significantly during putative electron transfer in the XFEL

218 structures (dataset b) (mV). The same residues are highlighted in the same colors for clarity.

Dataset b		shift		shift
0 to 1 ps	Ser-L238	8	Ser-L176	7
	B_L	-7	Leu-M213	-3
1 to 5 ps	Gly-M211	6	Leu-M213	5
	Ser-L238	-6	Thr-M253	-5
5 to 20 ps	B_L	12	Thr-M253	7
	Leu-M213	-4	P_M	-3
20 to 300 ps	Ser-L238	3	Gly-M211	2
	B_L	-10	Glu-L212	-4
300 ps to 8 μs	Glu-L212	4	Leu-M213	4
	B_L	-6	Gly-M211	-5

219

220 A normal-coordinate structural decomposition (NSD) analysis [9, 10] of the out-of-plane distortion of the

221 chlorin ring is sensitive to subtle structural changes in the chlorin ring, which are not distinct in the E_m

222 changes [6]. QM/MM calculations indicate that $H_L^{\bullet-}$ formation induces the saddling mode in the chlorin

223 ring, which describes the movement of rings I and III being in the opposite direction to the movement of

224 rings II and IV along the normal axis of the chlorin ring (Tables 5 and 6). However, (i) in the XFEL

225 structures, the saddling mode of H_L remains practically unchanged in dataset a during electron transfer

226 (Figure 6 and Tables S2 and S3). In dataset b, the saddling mode of H_L is induced most significantly at 1

227 ps, which does not correspond to the charge-separated $[P_LP_M]^{\bullet+}H_L^{\bullet-}$ state (Figure 7). (ii) In addition, the

228 ruffling mode is more pronounced than the saddling mode in H_L (Figure 7), which suggests that the

229 observed deformation of H_L is not directly associated with the reduction of H_L.

230

Table 5. Induced out-of-plane distortion of H_L and H_M in the PbRC protein environment of the dark structure for dataset a in response to the reduction (Å).

	saddling	**ruffling**	**doming**	**waving**		**propellering**
	B_{2u}	**B_{1u}**	**A_{2u}**	**$E_{g(x)}$**	**$E_{g(y)}$**	**A_{1u}**
H_L	0.18	0.35	-0.10	0.13	-0.11	0.13
$H_L^{\bullet-}$	0.24	0.35	-0.09	0.12	-0.12	0.13
($P_L^{\bullet+}H_L^{\bullet-}$)	(0.22)	(0.36)	(-0.07)	(0.13)	(-0.13)	(0.13)
$H_L/H_L^{\bullet-}$ difference	0.06	0.00	0.01	-0.01	-0.01	0.00
H_M	0.06	0.40	-0.20	0.37	0.12	0.19
$H_M^{\bullet-}$	0.12	0.38	-0.22	0.33	0.09	0.22
($P_L^{\bullet+}H_M^{\bullet-}$)	(0.14)	(0.38)	(-0.22)	(0.33)	(0.10)	(0.22)
$H_M/H_M^{\bullet-}$ difference	0.06	-0.02	-0.02	-0.04	-0.03	0.03

Table 6. Induced out-of-plane distortion of H_L and H_M in the PbRC protein environment of the dark structure for dataset b in response to the reduction (Å).

	saddling	**ruffling**	**doming**	**waving**		**propellering**
	B_{2u}	**B_{1u}**	**A_{2u}**	**$E_{g(x)}$**	**$E_{g(y)}$**	**A_{1u}**
H_L	0.13	0.35	-0.13	0.07	-0.09	0.20
$H_L^{\bullet-}$	0.25	0.34	-0.02	0.12	-0.16	0.13
($P_L^{\bullet+}H_L^{\bullet-}$)	(0.23)	(0.34)	(-0.03)	(0.12)	(-0.16)	(0.12)
$H_L/H_L^{\bullet-}$ difference	0.12	-0.01	0.11	0.05	-0.07	-0.07
H_M	0.08	0.57	-0.11	0.16	0.20	0.32
$H_M^{\bullet-}$	0.16	0.36	-0.19	0.36	0.18	0.21
($P_L^{\bullet+}H_M^{\bullet-}$)	(0.16)	(0.36)	(-0.20)	(0.36)	(0.18)	(0.21)
$H_M/H_M^{\bullet-}$ difference	0.08	-0.21	-0.08	0.20	-0.02	-0.11

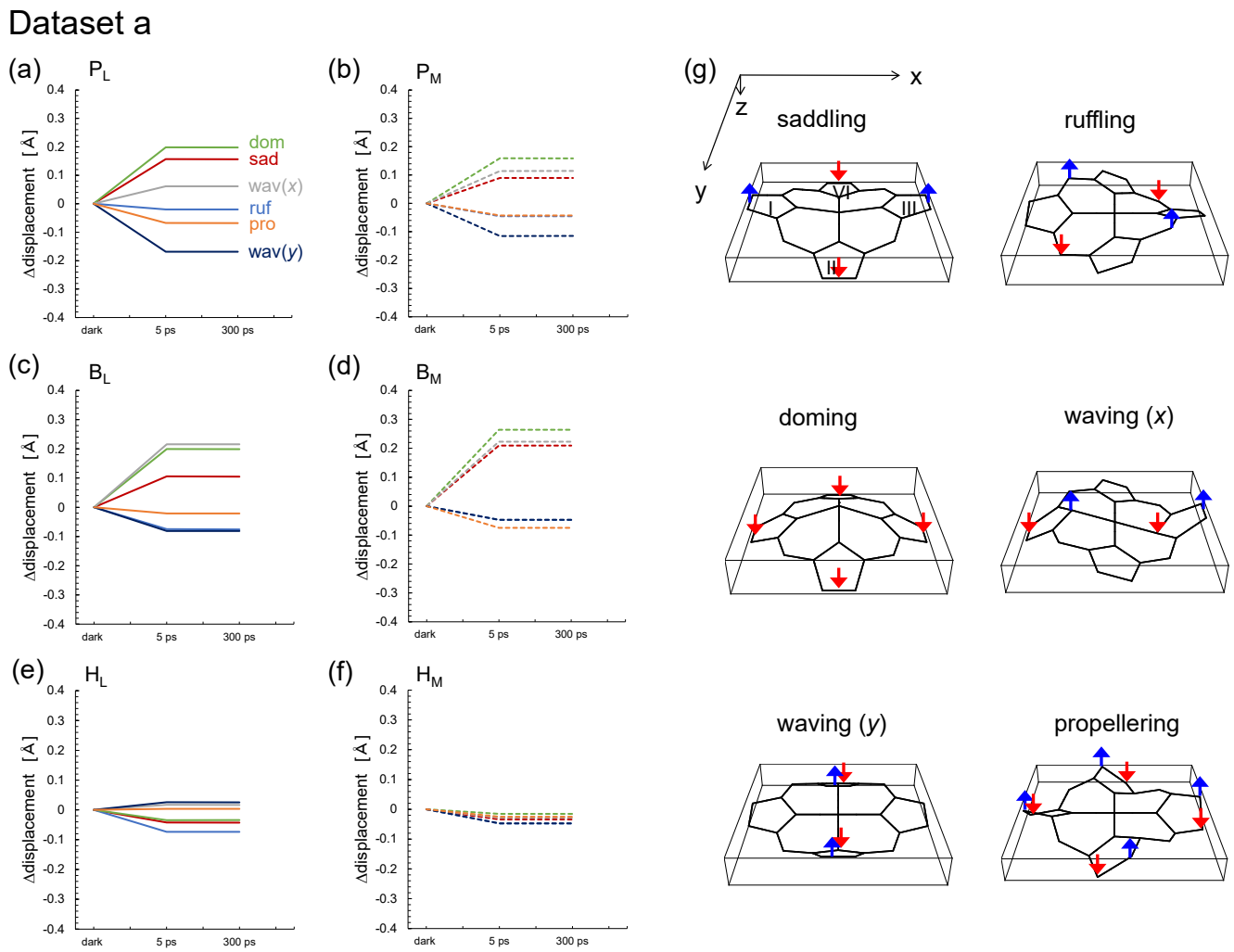

Figure 6. Time-dependent changes in the lowest frequency out-of-plane modes of the chlorin rings in the XFEL structures (dataset a). Sad: saddling (red); ruf: ruffling (blue); dom: doming (green); wav(x, y): waving (x, y) (gray, dark blue); pro: propellering (orange). Solid and dotted lines indicate L and M branches, respectively. See Table S2 for the absolute values in the dark state for dataset a.

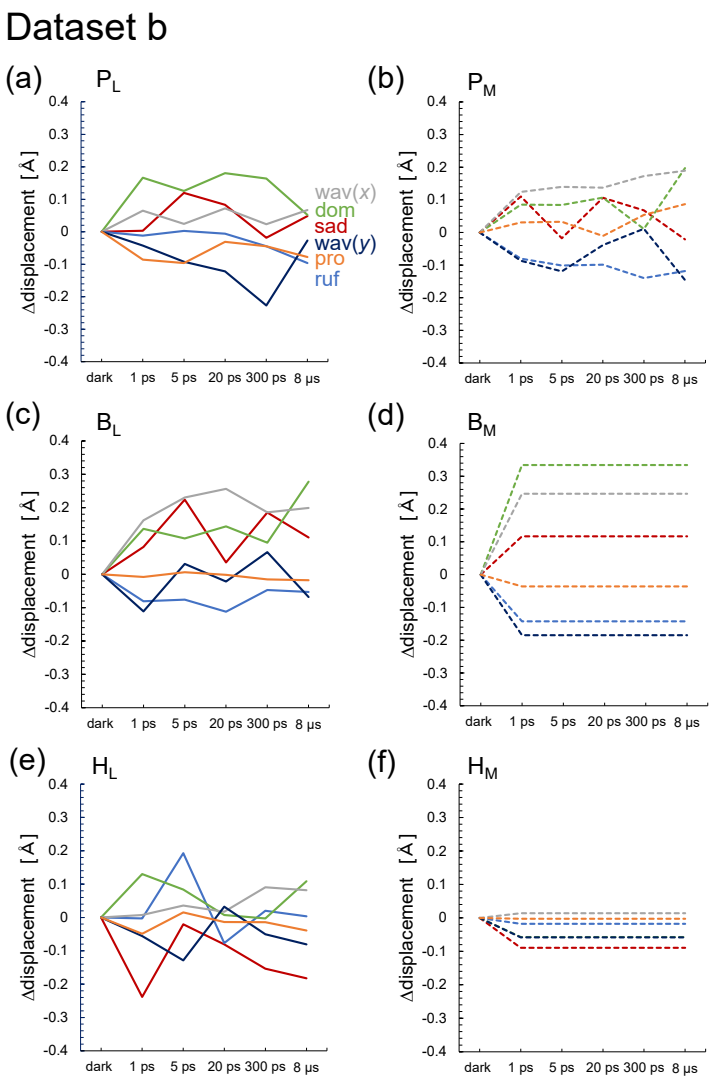

Figure 7. Time-dependent changes in the lowest frequency out-of-plane modes of the chlorin rings in the XFEL structures (dataset b). Sad: saddling (red); ruf: ruffling (blue); dom: doming (green); wav(x, y): waving (x, y) (gray, dark blue); pro: propellering (orange). Solid and dotted lines indicate L and M branches, respectively. See Table S3 for the absolute values in the dark state for dataset b.

One might argue that the loss of the link between the formation of the charge-separated state and the $E_m(H_L)$ change (Figure 5) is not due to experimental errors but rather represents the actual ps-timescale phenomena during the primary charge-separation reactions (e.g., Dods et al. noted that "the primary electron-transfer step to H_L is more rapid than conventional Marcus theory" [8]). However, even if this were the case, this hypothesis regarding the relevance of the XFEL structures to the electron-transfer events

could be further explored by examining the changes in $E_m(Q_A)$ among the XFEL structures, considering the relatively slow electron-transfer step to Q_A that allows sufficient protein relaxation to occur (e.g., Dods et al. stated that "the electron-transfer step to Q_A has a single exponential decay time of 230 ± 30 ps, consistent with conventional Marcus theory" [8]). That is, if the $E_m(Q_A)$ values are not higher in the 300-ps and 8-μs structures than in the other structures, it suggests that significant experimental errors exist, rendering the XFEL structures irrelevant to the electron transfer events. Consistent with this perspective, the present results demonstrate that the $E_m(Q_A)$ values in the 300-ps and 8-μs structures are not significantly higher than those in the other structures, including the dark state structure (Figure 8). Consequently, the lack of a clear relationship between the charge separated state and the changes in $E_m(Q_A)$ at 300 ps and 8-μs further strengthens the argument that the XFEL structures are irrelevant to the electron transfer events.

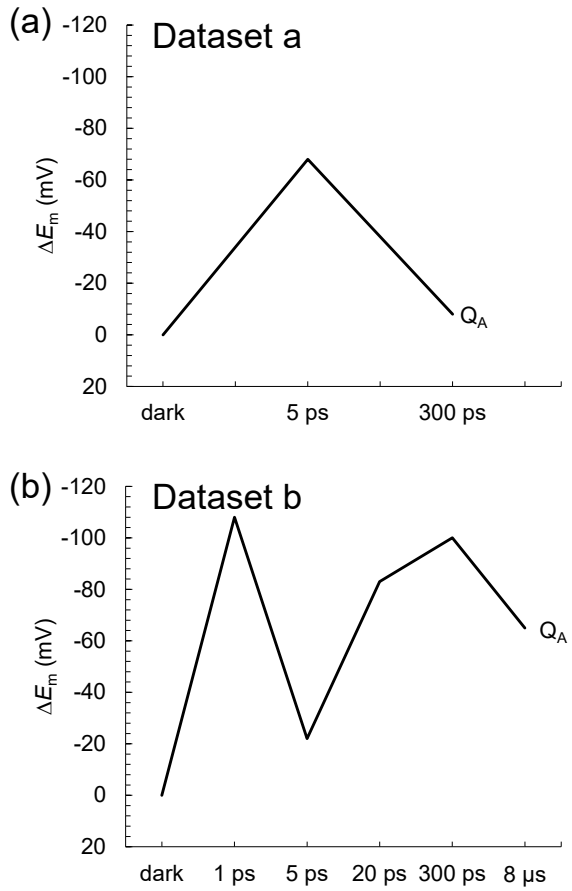

266 **Figure 8.** Time-dependent E_m changes for Q_A in the XFEL structures. (a) Dataset a. (b) Dataset b. ΔE_m
267 denotes the E_m shift with respect to the dark state structure. Note that the calculated $E_m(Q_A)$ values for
268 dataset a and dataset b in the dark structure are –223 mV and –209 mV, respectively, which are
269 comparable to experimentally measured values of –150 mV for PbRC from *Blastochloris viridis*
270 (menaquinone) [29] and –180 mV for PbRC from *Rhodobacter sphaeroides* (ubiquinone) [30].

271

272 In summary, the E_m values in the active L branch are higher than those in the inactive M branch in the
273 XFEL structures, which suggests that electron transfer via $B_L^{\bullet-}$ and $H_L^{\bullet-}$ is energetically more favored
274 than that via $B_M^{\bullet-}$ and $H_M^{\bullet-}$ (Figure 2). The Phe-L181/Tyr-M208 pair contributes to the difference between
275 $E_m(B_L)$ and $E_m(B_M)$ the most significantly, as observed in the Phe-L181/Tyr-M210 pair in PbRC from
276 *Rhodobacter sphaeroides* [13, 28]. The stabilization of the $[P_LP_M]^{\bullet+}H_L^{\bullet-}$ state owing to protein reorganization
277 is not clearly observed in the $E_m(H_L)$ values (Figure 5). The absence of the induced saddling mode in the
278 H_L chlorin ring in the 5- and 20-ps structures suggests that $H_L^{\bullet-}$ does not specifically exist in these XFEL
279 structures (Figures 6 and 7). The cyclic fluctuations in the contributions of the residues to $E_m(H_L)$ at
280 different time intervals suggest that the structural differences among the XFEL structures are not related
281 to the actual time course of charge separation (Table 4). The major limitation of the structural studies
282 conducted by Dods et al. [8] is the relatively low resolution of their XFEL structures, primarily at 2.8 Å.
283 Consequently, the observed changes in E_m values and chlorin ring deformations are more likely to reflect
284 experimental errors rather than actual structural changes induced by electron transfer events. This concern
285 is reinforced by the lack of a clear relationship between the actual $Q_A^{\bullet-}$ formation and the $E_m(Q_A)$ values
286 in the 300-ps and 8-μs structures (Figure 8). Consequently, the proposed time-dependent structural
287 changes proposed by Dods et al. [8] are highly likely irrelevant to the electron transfer events.

288 Hence, it is crucial to exercise caution when interpreting time-dependent XFEL structures, especially
289 in the absence of comprehensive evaluations of the energetics and accompanying structural changes. This
290 cautionary note should serve as a counterargument in the future, highlighting the potential pitfalls

associated with presenting time-dependent XFEL structures of insufficient quality and drawing conclusive interpretations of protein structural changes that may not be distinguishable from significant experimental errors. Future high-resolution structures may provide further insights into the actual structural changes relevant to electron transfer events. By combining both high-resolution structures and rigorous energetic evaluations, a more comprehensive understanding of the protein structure-function relationship can be achieved.

ACKNOWLEDGMENTS

This research was supported by JSPS KAKENHI (JP23H04963 to K.S.; JP20H03217 and JP23H02444 to H.I.) and Interdisciplinary Computational Science Program in CCS, University of Tsukuba.

Competing financial interests

The authors declare no financial and non-financial competing interests.

REFERENCES

1. Deisenhofer, J.; Epp, O.; Miki, K.; Huber, R.; Michel, H. (1985) Structure of the protein subunits in the photosynthetic reaction centre of *Rhodopseudomonas viridis* at 3 Å resolution, *Nature 318*, 618-624.
2. Rabenstein, B.; Ullmann, G. M.; Knapp, E.-W. (1998) Energetics of electron-transfer and protonation reactions of the quinones in the photosynthetic reaction center of *Rhodopseudomonas viridis*, *Biochemistry 37*, 2488-2495.
3. Kirmaier, C.; Laible, P. D.; Hanson, D. K.; Holten, D. (2003) B-side charge separation in bacterial photosynthetic reaction centers: nanosecond time scale electron transfer from H_B^- to Q_B, *Biochemistry 42*, 2016-2024.
4. Holzapfel, W.; Finkele, U.; Kaiser, W.; Oesterhelt, D.; Scheer, H.; Stilz, H. U.; Zinth, W. (1990) Initial electron-transfer in the reaction center from *Rhodobacter sphaeroides*, *Proc Natl Acad Sci U S A 87*, 5168-5172.
5. Marcus, R. A.; Sutin, N. (1985) Electron transfers in chemistry and biology, *Biochim. Biophys. Acta 811*, 265-322.
6. Saito, K.; Umena, Y.; Kawakami, K.; Shen, J. R.; Kamiya, N.; Ishikita, H. (2012) Deformation of chlorin rings in the photosystem II crystal structure, *Biochemistry 51*, 4290-4299.

7. Müh, F.; Williams, J. C.; Allen, J. P.; Lubitz, W. (1998) A conformational change of the photoactive bacteriopheophytin in reaction centers from *Rhodobacter sphaeroides*, *Biochemistry 37*, 13066-13074.
8. Dods, R.; Båth, P.; Morozov, D.; Gagnér, V. A.; Arnlund, D.; Luk, H. L.; Kübel, J.; Maj, M.; Vallejos, A.; Wickstrand, C.; Bosman, R.; Beyerlein, K. R.; Nelson, G.; Liang, M.; Milathianaki, D.; Robinson, J.; Harimoorthy, R.; Berntsen, P.; Malmerberg, E.; Johansson, L.; Andersson, R.; Carbajo, S.; Claesson, E.; Conrad, C. E.; Dahl, P.; Hammarin, G.; Hunter, M. S.; Li, C.; Lisova, S.; Royant, A.; Safari, C.; Sharma, A.; Williams, G. J.; Yefanov, O.; Westenhoff, S.; Davidsson, J.; DePonte, D. P.; Boutet, S.; Barty, A.; Katona, G.; Groenhof, G.; Brändén, G.; Neutze, R. (2021) Ultrafast structural changes within a photosynthetic reaction centre, *Nature 589*, 310-314.
9. Jentzen, W.; Song, X.-Z.; Shelnutt, J. A. (1997) Structural characterization of synthetic and protein-bound porphyrins in terms of the lowest-frequency normal coordinates of the macrocycle, *J Phys Chem B 101*, 1684-1699.
10. Shelnutt, J. A.; Song, X.-Z.; Ma, J.-G.; Jia, S.-L.; Jentzen, W.; Medforth, C. J. (1998) Nonplanar porphyrins and their significance in proteins, *Chem Soc Rev 27*, 31-41.
11. Brooks, B. R.; Bruccoleri, R. E.; Olafson, B. D.; States, D. J.; Swaminathan, S.; Karplus, M. (1983) CHARMM: a program for macromolecular energy minimization and dynamics calculations, *J. Comput. Chem. 4*, 187-217.
12. MacKerell, A. D., Jr.; Bashford, D.; Bellott, R. L.; Dunbrack, R. L., Jr.; Evanseck, J. D.; Field, M. J.; Fischer, S.; Gao, J.; Guo, H.; Ha, S.; Joseph-McCarthy, D.; Kuchnir, L.; Kuczera, K.; Lau, F. T. K.; Mattos, C.; Michnick, S.; Ngo, T.; Nguyen, D. T.; Prodhom, B.; Reiher, W. E., III; Roux, B.; Schlenkrich, M.; Smith, J. C.; Stote, R.; Straub, J.; Watanabe, M.; Wiorkiewicz-Kuczera, J.; Yin, D.; Karplus, M. (1998) All-atom empirical potential for molecular modeling and dynamics studies of proteins, *J. Phys. Chem. B 102*, 3586-3616.
13. Kawashima, K.; Ishikita, H. (2018) Energetic insights into two electron transfer pathways in light-driven energy-converting enzymes, *Chem Sci 9*, 4083-4092.
14. Kawashima, K.; Ishikita, H. (2017) Structural factors that alter the redox potential of quinones in cyanobacterial and plant photosystem I, *Biochemistry 56*, 3019-3028.
15. Bayly, C. I.; Cieplak, P.; Cornell, W. D.; Kollman, P. A. (1993) A well-behaved electrostatic potential based method using charge restraints for deriving atomic charges: the RESP model, *J. Phys. Chem. 97*, 10269-10280.
16. Jaguar. (2012), version 7.9, Schrödinger, LLC, New York, NY.
17. Bashford, D.; Karplus, M. (1990) Pkas of Ionizable Groups in Proteins - Atomic Detail from a Continuum Electrostatic Model, *Biochemistry 29*, 10219-10225.
18. Fajer, J.; Davis, M. S.; Brune, D. C.; Spaulding, L. D.; Borg, D. C.; Forman, A. (1976) Chlorophyll radicals and primary events, *Brookhaven Symp. Biol. 28*, 74.
19. Watanabe, T.; Kobayashi, M. (1991) Electrochemistry of chlorophylls, *in Chlorophylls (Scheer, H., Ed.)*, pp 287-303, CRC Press, Boca Raton, FL.
20. Kishi, S.; Saito, K.; Kato, Y.; Ishikita, H. (2017) Redox potentials of ubiquinone, menaquinone, phylloquinone, and plastoquinone in aqueous solution, *Photosynth Res 134*, 193-200.
21. Rabenstein, B.; Knapp, E. W. (2001) Calculated pH-dependent population and protonation of carbon-monoxy-myoglobin conformers, *Biophys. J. 80*, 1141-1150.
22. QSite. (2012), version 5.8, Schrödinger, LLC, New York, NY.
23. Humphrey, W.; Dalke, A.; Schulten, K. (1996) VMD: Visual molecular dynamics, *Journal of Molecular Graphics 14*, 33-38.
24. Zucchelli, G.; Brogioli, D.; Casazza, A. P.; Garlaschi, F. M.; Jennings, R. C. (2007) Chlorophyll ring deformation modulates Qy electronic energy in chlorophyll-protein complexes and generates spectral forms, *Biophys J 93*, 2240-2254.
25. Tamura, H.; Saito, K.; Ishikita, H. (2020) Acquirement of water-splitting ability and alteration of the charge-separation mechanism in photosynthetic reaction centers, *Proc Natl Acad Sci U S A 117*, 16373-16382.

26. Rutherford, A. W.; Heathcote, P.; Evans, M. C. W. (1979) Electron-paramagnetic-resonance measurements of the electron-transfer components of the reaction centre of *Rhodopseudomonas viridis*. Oxidation–reduction potentials and interactions of the electron acceptors, *Biochemical Journal 182*, 515-523.
27. Gunner, M. R.; Nicholls, A.; Honig, B. (1996) Electrostatic potentials in *Rhodopseudomonas viridis* reaction centers: implications for the driving force and directionality of electron transfer, *J. Phys. Chem. 100*, 4277-4291.
28. Parson, W. W.; Chu, Z.-T.; Warshel, A. (1990) Electrostatic control of charge separation in bacterial photosynthesis, *Biochim. Biophys. Acta 1017*, 251-272.
29. Prince, R. C.; Leigh, J. S.; Dutton, P. L. (1976) Thermodynamic properties of the reaction center of *Rhodopseudomonas viridis* in vivo measurement of the reaction center bacteriochlorophyll-primary acceptor intermediary electron carrier, *Biochim. Biophys. Acta 440*, 622-636.
30. Prince, R. C.; Dutton, P. L. (1976) The primary acceptor of bacterial photosynthesis: its operating midpoint potential?, *Arch. Biochem. Biophys. 172*, 329-334.